energies

MDPI

Article

Vibration Characteristics of a Hydroelectric Generating System with Different Hydraulic-Mechanical-Electric Parameters in a Sudden Load Increasing Process

Yixuan Guo [1,2], Xiao Liang [1,2], Ziyu Niu [1,2], Zezhou Cao [1,2], Liuwei Lei [1,2], Hualin Xiong [1,2] and Diyi Chen [1,2,*]

[1] Institute of Water Resources and Hydropower Research, Northwest A&F University, Xianyang 712100, China; yixuanguo@nwsuaf.edu.cn (Y.G.); xiaoliang824@nwsuaf.edu.cn (X.L.); niuziyu@nwsuaf.edu.cn (Z.N.); 1141065221@nwsuaf.edu.cn (Z.C.); liuweilei@nwsuaf.edu.cn (L.L.); xionghualin@nwafu.edu.cn (H.X.)
[2] Key Laboratory of Agricultural Soil and Water Engineering in Arid and Semiarid Areas, Ministry of Education, Northwest A&F University, Xianyang 712100, China
* Correspondence: diyichen@nwsuaf.edu.cn; Tel.: +86-181-6198-0277

Abstract: In a sudden load increasing process (SLIP), the hydroelectric generating system (HGS) experiences a severe vibration response due to the sudden change of the hydraulic-mechanical-electric parameters (HMEPs). The instability of HGS limits the ability of sudden load increase, and its flexibility and reliability are reduced. Thus, in this study, a new transient nonlinear coupling model of HGS is proposed, which couples the hydro-turbine governing system (HTGS) and the hydro-turbine generator shafting system (HGSS) with the hydraulic-mechanical-electric coupling force, rotating speed, flow rate, hydro-turbine torque, electromagnetic torque, and guide vane opening. By using numerical simulation, the influences of different HMEPs on the vibration characteristics of HGS in SLIP are analyzed. The result shows that, compared with stable operating conditions, the vibration amplitude of HGS increases sharply in SLIP. The increase of the sudden load increasing amount, blade exit flow angle, mass eccentricity and excitation current, and the decrease in guide bearing stiffness and average air gap between the stator and rotor cause abnormal vibration of different degrees in the HGS. Hydraulic factors have the greatest influence on the nonlinear dynamic behavior of HGS. The maximum vibration amplitude of HGS in SLIP is increased by 70.46%, compared with that under stable operating conditions. This study provides reasonable reference for the analysis of the nonlinear dynamic behavior of HGS in SLIP under the multiple vibration sources.

Keywords: hydroelectric generating system; sudden load increasing process; hydraulic-mechanical-electric parameters; nonlinear dynamics; vibration characteristics

Citation: Guo, Y.; Liang, X.; Niu, Z.; Cao, Z.; Lei, L.; Xiong, H.; Chen, D. Vibration Characteristics of a Hydroelectric Generating System with Different Hydraulic-Mechanical-Electric Parameters in a Sudden Load Increasing Process. *Energies* **2021**, *14*, 7319. https://doi.org/10.3390/en14217319

Academic Editor: Victor Becerra

Received: 12 October 2021
Accepted: 1 November 2021
Published: 4 November 2021

1. Introduction

Hydropower is an environmentally friendly renewable energy, which has been widely used all over the world, and is of great significance to sustainable development [1–3]. HGS has the benefits of a quick startup and shutdown, flexible scheduling, and low operating costs [4–6]. When HGSs regulate the peak and frequency of the power system, it is impossible to avoid a series of transient processes, such as load increase and decrease [7]. Although the duration of the transient process is short, the parameters of the hydro-turbine, governor, and pipe are abnormal due to the sudden load change [8]. Compared with the large power system, the sudden load change has a greater impact on single-machine single-load power systems (SMSLPSs), which aggravates the impact of HMEPs on HGS, and causes severe vibration of the HGS [9,10]. For example, the water hammer superimposition occurred in Tianshengqiao-II HGS in Guangxi, China, due to the poor guide vane opening and closing strategies, which resulted in damage to the hydro-turbine runner and the surge tank [11].

The vibration of HGS is mainly caused by three factors: hydraulic, mechanical, and electric [12,13]. For hydraulic factors, Zhuang et al. proposed a hydraulic unbalance force

model, and concluded that hydraulic factors determine the changing trend of HGSS dynamic behaviors [14]. Favrel et al. introduced a methodology to assess the vortex behavior, the pressure fluctuation, and the dynamic strain, and investigated the impact of precessing cavitation vortices on runner blades [15]. For mechanical factors, Al-Hussain et al. established a coupling model of lateral vibration and torsional vibration, and concluded that parallel misalignment is a source of both vibrations [16]. Yong-Wei T et al. established a coupling model of rub-induced force and temperature distribution, and found that the vibration and temperature increase when the rotor is running below its critical speed [17]. For electric factors, Calleecharan et al. derived an unbalanced magnetic pull (UMP) model, and found that the sensitivity of UMP to forcing frequency increases with the decrease in HGSS stiffness [18]. Xu et al. established a finite element rotor model and a UMP model, and concluded that UMP is limited by the saturation effects as the field current increases [19]. The above studies mainly focus on the vibration characteristics of HGS under stable operating conditions, and their application is limited. The transient process, as an important factor, effectively reflects the overall vibration characteristics of HGS.

In transient processes, the study of HGS vibration characteristics inevitably involves the time variant of parameters and the coupling of multi vibration sources due to the complex flow behavior [20,21]. Thus, the vibration characteristics of HGS in transient processes have not yet been further investigated. Zhang et al. established a hydraulic excitation model induced by a draft tube vortex, and analyzed the vibration characteristics of HGS in a sudden load increase of 10% [22]. Wu et al. proposed a coupling structure model of HGSS and the powerhouse, and researched the vibration characteristics of HGSS under mechanical and electromagnetic factors under start-up conditions [23]. The above studies only analyzed single or double vibration sources, but did not fully study the comprehensive influences of HMEPs on HGS vibration characteristics. Guo et al. established an HGSS model by using the dual-disc rotor system, and explored the vibration characteristics of the generator rotor and the hydro-turbine runner during the load rejection [24]. Although the simplified dual-disc rotor system reflects the vibration characteristics of the generator rotor and hydro-turbine runner, the vibration characteristics of other key parts of the HGSS, such as the guide bearing, are not obtained. In addition, the simplification of the model causes calculation errors.

Thus, this study proposes a new transient nonlinear coupling model of HGS, which couples HTGS and HGSS. The model is modularized, based on the real HGS parameters of China. The sub-models include: the water diversion system (WDS) model established by the method of characteristics (MOC), the generator and load model, the PID governor model, the hydro-turbine model and HGSS model established by the Riccati transfer matrix method (RTMM), and the Wilson-θ numerical integration method (WNIM). Through numerical simulation, the influences of different HMEPs on the vibration characteristics of HGS in SLIP under SMSLPS are investigated.

The innovations of this study lie in three main aspects: (1) a new coupling method is proposed, which adds HGSs, a hydro-turbine characteristic curve, and a PID governor to the HGS model; (2) the vibration characteristics of HGSS in SLIP are studied, which have not yet been further investigated; (3) considering the hydraulic-mechanical-electric coupling vibration source, the influences of different HMEPs on the vibration characteristics of HGS in SLIP are studied.

The structure of this paper is as follows: in Section 2, the transient nonlinear coupling model of HGS is established and verified. Section 3 analyzes the influences of different HMEPs on the vibration characteristics of HGSS in SLIP under SMSLPS. Finally, in Section 4, the main results are summarized.

2. Transient Nonlinear Coupling Model of HGS

The HGS is composed of an upstream reservoir, a diversion tunnel, a surge tank, a pipe, an HGSS, a draft tube, and a downstream reservoir. The schematic diagram of the HGS is shown in Figure 1. The transient nonlinear coupling model of the HGS is

established through the coupling of a hydro-turbine and the WDS, and the coupling of HTGS and HGSS. The schematic diagram of the HGS coupling model is shown in Figure 2.

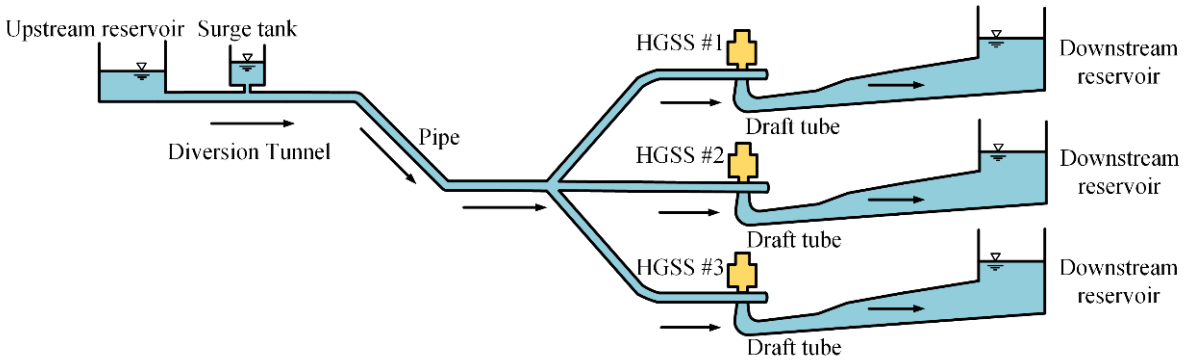

Figure 1. The schematic diagram of the HGS.

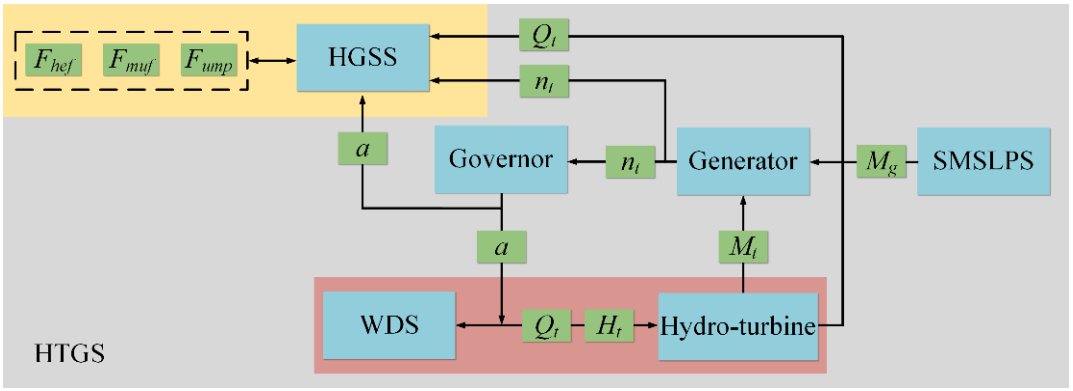

Figure 2. The schematic diagram of the HGS transient nonlinear coupling model.

2.1. Model of WDS

The WDS is composed of a reservoir, a diversion tunnel, a surge tank, and a pipe. MOC is used to transform the partial differential equation of the unsteady flow into an ordinary differential equation, and then the ordinary differential equation is approximately transformed into a differential equation for hydraulic transient analysis [25,26]. The hydraulic transient motion equation L_1 and the continuous equation L_2 are:

$$\begin{cases} L_1 = \frac{\partial H}{\partial X} + \frac{V}{g}\frac{\partial V}{\partial X} + \frac{1}{g}\frac{\partial V}{\partial t} + \frac{f|V|V}{2gD} = 0 \\ L_2 = \frac{\partial H}{\partial t} + V\frac{\partial H}{\partial X} + \frac{{a_w}^2}{g}\frac{\partial V}{\partial X} + V\sin\sigma = 0 \end{cases} \quad (1)$$

where H is the water head; X is the pipe length; V is the flow velocity; g is the gravitational acceleration; t is the time; f is the Darcy–Weisbach friction coefficient; D is the pipe diameter; a_w is the pressure wave velocity; and σ is the angle of the pipe inclined with the horizontal.

Equation (1) is solved by MOC combined with boundary conditions. The schematic diagram of MOC is shown in Figure 3. The flow rate and the water head at point p are calculated through the flow rate and the water head at point d and u, which are shown in Equations (2) and (3). More detailed descriptions of MOC are obtained in [27].

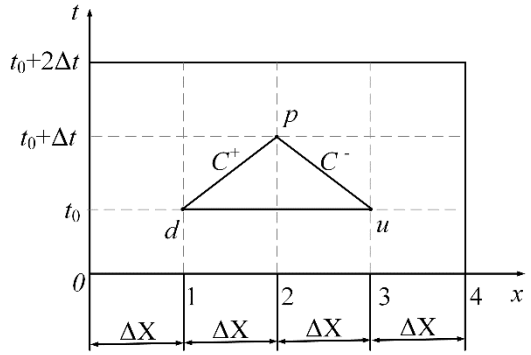

Figure 3. The schematic diagram of MOC.

$$\begin{cases} C^+ : Q_p = C_p - C_a H_p \\ C^- : Q_p = C_n + C_a H_p \end{cases} \tag{2}$$

$$\begin{cases} C_a = \frac{gA}{a_w} \\ C_p = Q_d + \frac{gA}{a_w} H_d - \frac{f\Delta t}{2DA} Q_d |Q_d| + \frac{Q_d \Delta t g}{{a_w}^2} \sin\sigma \\ C_n = Q_u - \frac{gA}{a_w} H_u - \frac{f\Delta t}{2DA} Q_u |Q_u| - \frac{Q_u \Delta t g}{{a_w}^2} \sin\sigma \end{cases} \tag{3}$$

where Q_p, Q_d, Q_u, H_p, H_d, and H_u are the flow rate and the water head at point p, d, and u, respectively; C_a, C_p, and C_n are intermediate variables; A is the cross-sectional area of the pipe; Δt is the time step.

2.2. The Boundary Conditions of WDS

When the WDS model established in 2.1 is used to calculate the flow rate and the water head at each point of the pipe, the corresponding boundary conditions are required. The schematic diagram of boundary conditions for each node of the WDS is shown in Figure 4.

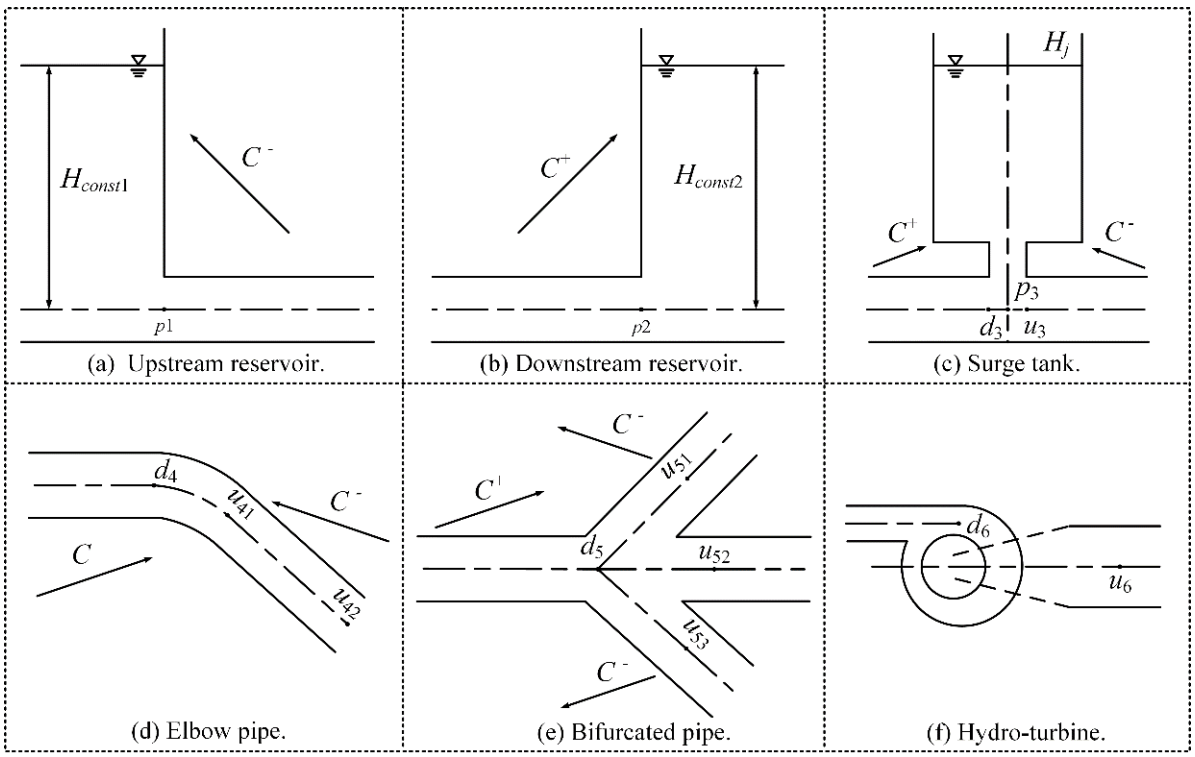

Figure 4. The schematic diagram of boundary conditions for each node of the WDS.

(1) Upstream and downstream reservoirs

Considering the large area of the reservoir, it is assumed that the water levels of the upstream and downstream reservoirs are constant during the transient flow, and the pipe inlet head loss is ignored. The boundary conditions of the upstream and downstream reservoirs are [28]:

$$\begin{cases} H_{p1} = H_{const1} \\ Q_{p1} = C_{n1} + C_{a1} H_{p1} \end{cases} \tag{4}$$

$$\begin{cases} H_{p2} = H_{const2} \\ Q_{p2} = C_{p2} - C_{a2} H_{p2} \end{cases} \tag{5}$$

where Q_{p1} and Q_{p2} are the flow rate at points p_1 and p_2, respectively; H_{p1} and H_{p2} are the water head at p_1 and p_2, respectively; H_{const1} and H_{const2} are the water head of upstream reservoir and downstream reservoir, respectively; and C_{n1}, C_{p2}, C_{a1}, and C_{a2} are intermediate variables.

(2) Surge tank

To reduce the water hammer pressure of the pipe in the transient process, a surge tank is built at the connection between the pressure diversion channel and the penstock for long WDS. The mathematical model is described in [29]. The boundary condition of surge tank is:

$$\begin{cases} Q_{d3} = C_{p3} - C_{a31} H_{d3} \\ Q_{u3} = C_{n3} + C_{a32} H_{u3} \\ Q_{d3} = Q_j + Q_{u3} \\ H_{d_3} = H_{u_3} = H_{p3} \\ H_{p3} = H_j + R_j \frac{Q_j |Q_j|}{A_{wj}^2} \\ H_j = H_{j,\Delta t} + \frac{(Q_j + Q_{j,\Delta t})\Delta t}{2A_j} \end{cases} \tag{6}$$

where Q_{d3} and Q_{u3} are the flow rate at points d_3 and u_3, respectively; H_{d3} and H_{u3} are the water head at points d_3 and u_3, respectively; C_{p3}, C_{n3}, C_{a31}, and C_{a32} are intermediate variables; Q_j and $Q_{j,\Delta t}$ are the surge tank flow rate at this moment and the last moment, respectively; H_j and $H_{j,\Delta t}$ are the surge tank water level at this moment and the last moment, respectively; H_{p3} is the water head at point p_3; R_j is the hydraulic loss coefficient of surge tank inlet impedance; A_{wj} is the cross-sectional area of the impedance hole; and A_j is the cross-sectional area of surge tank.

(3) Elbow pipe and bifurcated pipe

The front and rear sections of the elbow pipe satisfy the characteristic equation. The elbow pipe also satisfies the flow rate and water head balance equation, as shown in Equation (7). The boundary condition of elbow pipe is [29]:

$$\begin{cases} Q_{d4} = C_{p4} - C_{a41} H_{d4} \\ Q_{u41} = C_{n4} + C_{a42} H_{u41} \\ Q_{u41} = Q_{u42} \\ H_{u41} = H_{u42} + \xi \frac{V_{u42}^2}{2g} \end{cases} \tag{7}$$

where Q_{d4}, Q_{u41} and Q_{u42} are the flow rate at points d_4, u_{41}, and u_{42}, respectively; H_{d4}, H_{u41}, and H_{u42} are the water head at points d_4, u_{41}, and u_{42}, respectively; C_{p4}, C_{n4}, C_{a41}, and C_{a42} are intermediate variables; ξ is the local head loss coefficient; and V_{u42} is the flow velocity at point u_{42}.

The front and rear sections of the bifurcated pipe satisfy the characteristic equation. The head loss at the joint is ignored. According to the energy equation and continuity equation, the boundary condition of the bifurcated pipe is [29]:

$$\begin{cases} Q_{d5} = C_{p5} - C_{a5}H_{d5} \\ Q_{u51} = C_{n51} + C_{a51}H_{u51} \\ Q_{u52} = C_{n52} + C_{a52}H_{u52} \\ Q_{u53} = C_{n53} + C_{a53}H_{u53} \\ H_{d5} = H_{u51} = H_{u52} = H_{u53} = H_p \\ Q_{d5} = Q_{u41} + Q_{u52} + Q_{u53} \end{cases} \tag{8}$$

where Q_{d5}, Q_{u51}, Q_{u52}, and Q_{u53} are the flow rate at points d_5, u_{51}, u_{52}, and u_{53}, respectively; H_{d5}, H_{u51}, H_{u52}, and H_{u53} are the water head at points d_5, u_{51}, u_{52}, and u_{53}, respectively; C_{p5}, C_{n51}, C_{n52}, C_{n53}, C_{a5}, C_{a51}, C_{a52}, and C_{a53} are intermediate variables.

(4) Hydro-turbine

The water head of the hydro-turbine is the difference between the inlet of the volute and the outlet of the draft tube. The flow loss of the hydro-turbine is ignored. The boundary condition of the hydro-turbine is [24]:

$$\begin{cases} Q_{d6} = Q_{u6} = Q_t \\ Q_{d6} = C_{p6} - C_{a61}H_{d6} \\ Q_{u6} = C_{n6} + C_{a62}H_{u6} \\ H_t = H_{d6} - H_{u6} \end{cases} \tag{9}$$

where Q_{d6} and Q_{u6} are the flow rate at points d_6 and u_6, respectively; H_{d6} and H_{u6} are the water head at points d_6 and u_2, respectively; C_{p6}, C_{n6}, C_{a61}, and C_{a62} are intermediate variables; and Q_t is the flow rate of the hydro-turbine, which is obtained from the hydro-turbine model.

2.3. Model of Hydro-Turbine

The modeling process of the hydro-turbine depends on the characteristic curve of hydro-turbine, as the boundary of the pipe, its characteristics need to be. When the guide vane opening, rotating speed, and water head are known, the characteristic line equation of the pipe is solved simultaneously. The hydro-turbine characteristic data are transformed into characteristic curves through the polynomial interpolation method, as shown in Figure 5. The calculation formulas of the flow rate, torque, and speed are [30]:

$$\begin{cases} Q_{11} = f(n_{11}, a), Q_t = Q_{11}D_1^2\sqrt{H_t} \\ M_{11} = f(n_{11}, a), M_t = M_{11}D_1^3H_t \\ n_t = \frac{n_{11}\sqrt{H_t}}{D_1} \end{cases} \tag{10}$$

where Q_{11} is the unit flow rate; M_{11} is the unit torque; n_{11} is the unit rotating speed; and a is the guide vane opening.

2.4. Model of Generator and Load

In this study, the parallel operation of the HGSS is regarded as a rotating rigid body, and electromagnetic power, torque angle, and the change of the field winding flux are not considered. Thus, the first-order generator model is selected. In addition, HGSS still bears the grid load, and the generator electromagnetic torque is not zero in SLIP. The model of generator and load [31] is:

$$\begin{cases} M_t - M_g = J\frac{d\omega}{dt} \\ m_g = C_g + A_g + e_g(n - n_r) \\ n_t = n_{(t-\Delta t)} + \frac{\Delta t}{T_a}\left[1.5\left(m_{t(t-\Delta t)} - m_{g(t-\Delta t)}\right) - 0.5\left(m_{t(t-2\Delta t)} - m_{g(t-2\Delta t)}\right)\right] \end{cases} \tag{11}$$

where M_t is the driving torque; M_g is the electromagnetic torque; ω is the angular velocity; J is the moment of inertia; m_g is the relative electromagnetic torque; C_g is the relative load torque; A_g is the step value of load torque; n_r is the relative rated speed; e_g is the load self-regulation coefficient; n is the relative rotating speed; and T_a is the inertia time constant.

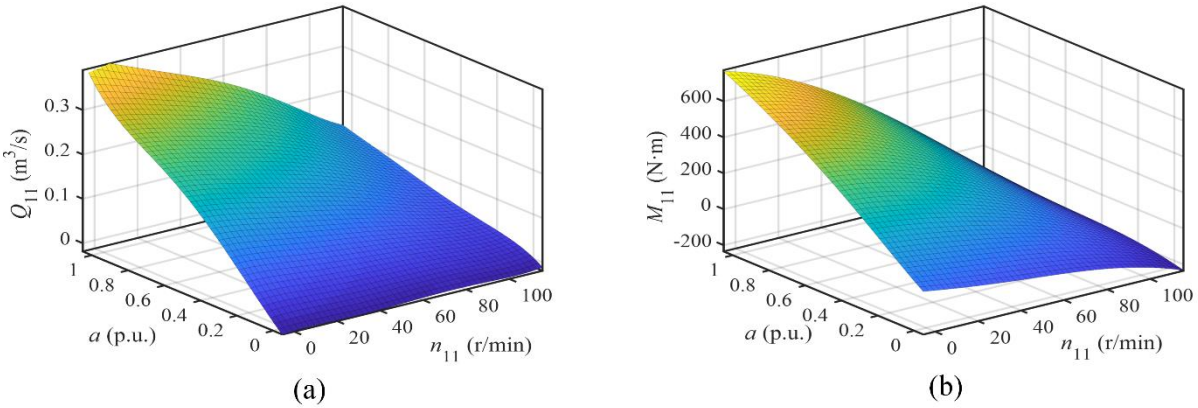

Figure 5. The characteristics of hydro-turbine. (**a**) The flow rate; (**b**) the torque.

2.5. Model of PID Governor

In SLIP, the control mode of HGS is changed to frequency control under SMSLPS in order to ensure that the HGS tracks the load change automatically, and maintains the frequency near the rated frequency [32]. Where K_P, K_I, and K_D are the proportional, integral, and differential coefficients, respectively; x_1 is the intermediate variable; x_2 is the output variable; T_y is the servomotor response time; and b_p is the permanent difference coefficient. The equations are shown in Equations (12) and (13) [33]. The schematic diagram of the PID governor is shown in Figure 6.

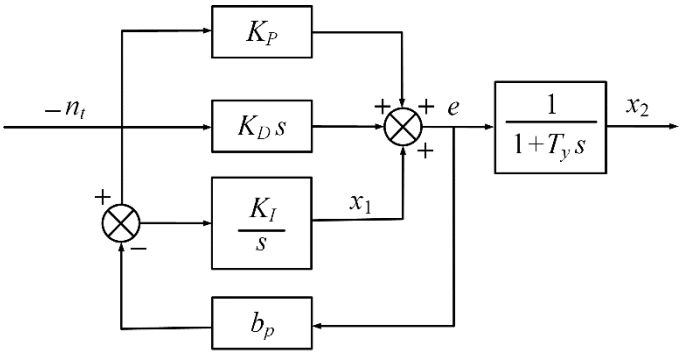

Figure 6. The schematic diagram of the PID governor.

$$\begin{cases} \dot{x}_1 = -K_I n_t - b_p e \\ \dot{x}_2 = -\frac{1}{T_y} x_2 + \frac{1}{T_y} e \end{cases} \tag{12}$$

$$e = x_1 - K_P n_t - K_D \dot{n}_t \tag{13}$$

When transformed in Equations (12) and (13), the state equation of the PID governor model is:

$$\begin{bmatrix} \dot{x}_1 \\ \dot{x}_2 \end{bmatrix} = \begin{bmatrix} -b_p & 0 \\ 1/T_y & -1/T_y \end{bmatrix} \begin{bmatrix} x_1 \\ x_2 \end{bmatrix} + \begin{bmatrix} b_p K_P - K_I & b_p K_D \\ -K_P/T_y & -K_D/T_y \end{bmatrix} \begin{bmatrix} n_t \\ \dot{n}_t \end{bmatrix} \tag{14}$$

2.6. Model of HGSS

The HGSS is composed of runners, turbine shafts, generator shafts, generator rotors, and guide bearings. This study discretizes the vertical HGSS with a continuous mass distribution, and transforms it into a multi degree of freedom nodes with the centralized mass and the centralized moment of inertia [34]. These nodes are generally selected in the generator rotors, bearings, runners, and shaft diameter changes. In this section, the structural model of HGSS is established through the combination of RTMM and WNIM. The HGSS is divided into 18 nodes and 17 shaft segments for modeling. The schematic diagram of the HGSS is shown in Figure 7.

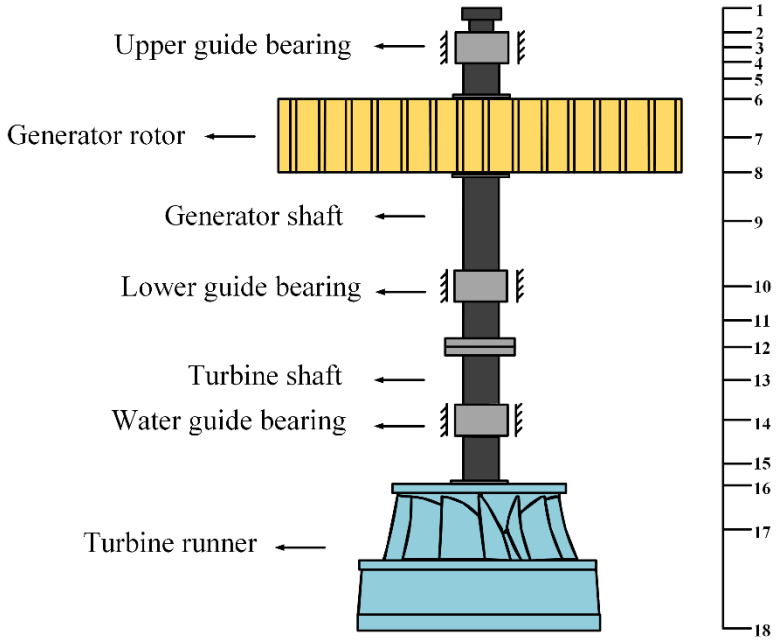

Figure 7. The schematic diagram of the HGSS.

(1) WNIM

WNIM is a stepwise integration method. The displacements of each node at time $t + \theta\Delta t$ and the displacements, velocities, and accelerations of each node at time t are known to obtain the displacements, velocities, and accelerations of each node at time $t + \Delta t$ [35]. The expression of WNIM is

$$\begin{cases} \ddot{x}_{t+\Delta t} = \frac{6}{\theta^3\Delta t^2}(x_{t+\theta\Delta t} - x_t) - \frac{6}{\theta^2\Delta t}\dot{x}_t + (1 - \frac{3}{\theta})\ddot{x}_t \\ \dot{x}_{t+\Delta t} = \dot{x}_t + \frac{\Delta t}{2}(\ddot{x}_{t+\Delta t} + 2\ddot{x}_t) \\ x_{t+\Delta t} = x_t + \dot{x}_t\Delta t + \frac{\Delta t^2}{6}(\ddot{x}_{t+\Delta t} + 2\ddot{x}_t) \end{cases} \tag{15}$$

where x is the displacement. When $\theta \geq 1.37$, WNIM is unconditionally stable.

(2) Differential equations of motion:

$$\begin{cases} m_i \begin{Bmatrix} \ddot{x} \\ \ddot{y} \end{Bmatrix}_i = -\begin{bmatrix} K_{xx} & K_{xy} \\ K_{yx} & K_{yy} \end{bmatrix}_i \begin{Bmatrix} x \\ y \end{Bmatrix}_i - \begin{bmatrix} C_{xx} & C_{xy} \\ C_{yx} & C_{yy} \end{bmatrix}_i \begin{Bmatrix} \dot{x} \\ \dot{y} \end{Bmatrix}_i + \begin{Bmatrix} P_x^L - P_x^R \\ P_y^L - P_y^R \end{Bmatrix}_i + \begin{Bmatrix} F_x(t) \\ F_y(t) \end{Bmatrix}_i \\ J_{di} \begin{Bmatrix} \ddot{\varphi} \\ \ddot{\psi} \end{Bmatrix}_i = -\omega \begin{bmatrix} 0 & J_p \\ -J_p & 0 \end{bmatrix}_i \begin{Bmatrix} \dot{\varphi} \\ \dot{\psi} \end{Bmatrix}_i + \begin{Bmatrix} M_x^R - M_x^L \\ M_y^R - M_y^L \end{Bmatrix}_i + \begin{Bmatrix} L_{ax}(t) \\ L_{ay}(t) \end{Bmatrix}_i \end{cases} \tag{16}$$

where subscripts i, x, y, d, and p are the ith node, x-direction, y-direction, radial direction and axial direction, respectively; superscripts L and R are the left and right sections of each node; m is the mass; x, y, ψ, and φ are the displacements; K is the stiffness coefficient; C is the damping coefficient; P and M are the shear force and the shear moment, respectively; and F_a and L_a are additional forces and additional moments, respectively.

(3) RTMM

The state vectors of each node are divided into $f = \{M_x, Q_x, M_y, Q_y\}^{\mathrm{T}}$ and $e = \{x, y, \psi, \varphi\}^{\mathrm{T}}$. Combined with the differential equation of motion, the transfer matrix at time $t + \theta\Delta t$ is:

$$\begin{Bmatrix} f \\ e \end{Bmatrix}_{i+1} = \begin{bmatrix} B_{11} & B_{12} \\ B_{21} & B_{22} \end{bmatrix} \begin{bmatrix} T_{11} & T_{12} \\ T_{21} & T_{22} \end{bmatrix} \begin{Bmatrix} f \\ e \end{Bmatrix}_i + \begin{Bmatrix} T_{13} \\ T_{23} \end{Bmatrix}_i = \begin{bmatrix} u_{11} & u_{12} \\ u_{21} & u_{22} \end{bmatrix} \begin{Bmatrix} f \\ e \end{Bmatrix}_i + \begin{Bmatrix} F_f \\ F_e \end{Bmatrix}_i \tag{17}$$

$$[u_{22}]_i = [B_{21}]_i[T_{12}]_i + [B_{22}]_i, \left\{F_f\right\}_i = [B_{11}]_i\{T_{13}\}_i, \{F_e\}_i = [B_{21}]_i\{T_{13}\}_i, [T_{23}] = \begin{Bmatrix} 0 & 0 & 0 & 0 \end{Bmatrix}^T,$$

$$[T_{11}]_i = [T_{22}]_i = \begin{bmatrix} 1 & 0 & 0 & 0 \\ 0 & 1 & 0 & 0 \\ 0 & 0 & 1 & 0 \\ 0 & 0 & 0 & 1 \end{bmatrix}, [T_{12}]_i = \begin{bmatrix} 0 & K_2 & 0 & K_3 \\ W_1 & 0 & W_2 & 0 \\ 0 & -K_3 & 0 & K_2 \\ W_3 & 0 & W_4 & 0 \end{bmatrix}, [B_{11}]_i = [B_{22}]_i = [u_{11}]_i = \begin{bmatrix} 1 & l & 0 & 0 \\ 0 & 1 & 0 & 0 \\ 0 & 0 & 1 & l \\ 0 & 0 & 0 & 1 \end{bmatrix},$$

$$[u_{12}]_i = \begin{bmatrix} lW_1 & K_2 & lW_2 & K_3 \\ W_1 & 0 & W_2 & 0 \\ lW_3 & -K_3 & lW_4 & K_2 \\ W_3 & 0 & W_4 & 0 \end{bmatrix}, [B_{21}]_i = [u_{21}]_i = \begin{bmatrix} a_2 & a_3 & 0 & 0 \\ a_1 & a_2 & 0 & 0 \\ 0 & 0 & a_2 & a_3 \\ 0 & 0 & a_1 & a_2 \end{bmatrix}, \tag{18}$$

$$[T_{13}] = \begin{Bmatrix} -K_2\varphi_t - \frac{6J_{di}}{\theta\Delta t}\dot{\varphi}_t - 2J_{di}\ddot{\varphi}_t - K_3\psi_t - 2J_{pi}\omega\dot{\psi}_t - \frac{1}{2}J_{pi}\omega\theta\Delta t\ddot{\psi}_t - L_x(t+\theta\Delta t) \\ (2m + \frac{1}{2}\theta\Delta tC_{xx})\ddot{x}_t + \frac{1}{2}\theta\Delta tC_{xy}\ddot{y}_t + (\frac{6m}{\theta\Delta t} + 2C_{xx})\dot{x}_t + 2C_{xy}\dot{y}_t + (\frac{6m}{(\theta\Delta t)^2} + \frac{3C_{xx}}{\theta\Delta t})x_t + \frac{3}{\theta\Delta t}C_{xy}y_t + F_x(t+\theta\Delta t) \\ -K_2\psi_t - \frac{6J_{di}}{\theta\Delta t}\dot{\psi}_t - 2J_{di}\ddot{\psi}_t + K_3\varphi_t + 2J_{pi}\omega\dot{\varphi}_t + \frac{1}{2}J_{pi}\omega\theta\Delta t\ddot{\varphi}_t - L_y(t+\theta\Delta t) \\ (2m + \frac{1}{2}\theta\Delta tC_{yy})\ddot{y}_t + \frac{1}{2}\theta\Delta tC_{yx}\ddot{x}_t + (\frac{6m}{\theta\Delta t} + 2C_{yy})\dot{y}_t + 2C_{yx}\dot{x}_t + (\frac{6m}{(\theta\Delta t)^2} + \frac{3C_{yy}}{\theta\Delta t})y_t + \frac{3}{\theta\Delta t}C_{yx}x_t + F_y(t+\theta\Delta t) \end{Bmatrix},$$

$$K_1 = \frac{6m_i}{(\theta\Delta t)^2}, K_2 = \frac{6J_{di}}{(\theta\Delta t)^2}, K_3 = \frac{3J_{pi}\omega}{\theta\Delta t}, W_1 = -K_{xx} - \frac{3}{\theta\Delta t}C_{xx} - \frac{6m}{(\theta\Delta t)^2}, W_2 = -K_{xy} - \frac{3}{\theta\Delta t}C_{xy},$$
$$W_3 = -K_{yx} - \frac{3}{\theta\Delta t}C_{yx}, W_4 = -K_{yy} - \frac{3}{\theta\Delta t}C_{yy} - \frac{6m}{(\theta\Delta t)^2}, a_1 = \frac{l}{EJ}, a_2 = \frac{l^2}{2EJ}, a_3 = \frac{l^3}{6EJ}. \tag{19}$$

where l is the length of the shaft segment; and EJ is the bending stiffness.

The Riccati transformation is:

$$\{f\}_i = [S]_i\{e\}_i + \{P\}_i \tag{20}$$

where $[S]_i$ and $\{p\}_i$ are the undetermined matrices.

It is obtained from Equations (17) and (20):

$$\begin{cases} [S]_{i+1} = [u_{11}S + u_{12}]_i[u_{21}S + u_{22}]_i^{-1} \\ \{P\}_{i+1} = \left\{u_{11}P + F_f\right\}_i - [S]_{i+1}[u_{21}P + F_e]_i \end{cases} \tag{21}$$

From the boundary conditions $\{f\}_1 = 0$ and $\{e\}_1 \neq 0$, $[S]_1 = 0$ and $\{p\}_1 = 0$ is obtained. In addition, from Equation (21), $[S]_i$ and $\{p\}_i$ are obtained. The boundary condition $\{f\}_{N+1} = 0$ and Equation (21) are combined to obtain:

$$\{e\}_{N+1} = -[S]_{N+1}^{-1}\{P\}_{N+1} \tag{22}$$

Thus, the displacements of each node at time $t + \theta\Delta t$ are obtained:

$$\{e\}_i = [u_{21}S + u_{22}]_i^{-1}(\{e\}_{i+1} - [u_{21}P + F_e]_i) \tag{23}$$

2.7. Additional Forces on HGSS

(1) Nonlinear oil film force

Most of the guide bearings on HGSS are oil-lubricated sliding bearings with tilting pads. The oil film force of the bearing has a non-linear relationship with the speed and displacement of the journal. The expression of nonlinear oil film force [36] is:

$$\begin{Bmatrix} F_x \\ F_y \end{Bmatrix} = \sigma \cdot \begin{Bmatrix} f_x \\ f_y \end{Bmatrix} = -\frac{\left[(x-2y')^2 + (y+2x')^2\right]^{1/2}}{1-x^2-y^2} \cdot \begin{Bmatrix} 3x \cdot V(x,y,\alpha) - \sin\alpha \cdot G(x,y,\alpha) - 2\cos\alpha \cdot S(x,y,\alpha) \\ 3y \cdot V(x,y,\alpha) + \cos\alpha \cdot G(x,y,\alpha) - 2\sin\alpha \cdot S(x,y,\alpha) \end{Bmatrix} \tag{24}$$

$$V(x,y,\alpha) = \frac{2 + (y\cos\alpha - x\sin\alpha)\cdot G(x,y,\alpha)}{1 - x^2 - y^2} \tag{25}$$

$$G(x,y,\alpha) = \frac{2}{(1-x^2-y^2)^{1/2}}\left[\frac{\pi}{2} + \arctan\frac{y\cos\alpha - x\sin\alpha}{(1-x^2-y^2)^{1/2}}\right] \tag{26}$$

$$S(x,y,\alpha) = \frac{x\cos\alpha + y\sin\alpha}{1 - (x\cos\alpha + y\sin\alpha)^2} \tag{27}$$

$$\alpha = \arctan\frac{y+2x'}{x-2y'} - \frac{\pi}{2}\mathrm{sgn}\left(\frac{y+2x'}{x-2y'}\right) - \frac{\pi}{2}\mathrm{sgn}(y+2x') \tag{28}$$

$$\sigma = \mu\omega R_b L_b \left(\frac{R_b}{C_b}\right)^2 \left(\frac{L_b}{D_b}\right)^2 \tag{29}$$

where μ is the lubricating oil viscosity; R_b is the guide bearing radius; L_b is the guide bearing length; C_b is the guide bearing clearance; and D_b is the guide bearing diameter.

(2) Mechanical unbalance force

Due to uneven mass distribution and installation accuracy, mass eccentricity occurs at the generator rotor and the hydro-turbine runner, which causes the rotation center to shift. The expression of mechanical unbalance force [37] is:

$$F_{muf} = me\omega^2 \tag{30}$$

where F_{muf} is the mechanical unbalance force; and e is the eccentricity.

(3) UMP

When the air gap between the stator and the rotor is uneven due to manufacturing or installation errors, the rotor produces a lateral unbalanced magnetic tension. The expression of UMP [38] is:

$$\begin{cases} F_{x-ump} = \frac{R_r L_r \pi}{4\mu_0} {F_j}^2 (2\Lambda_0\Lambda_1 + \Lambda_1\Lambda_2 + \Lambda_2\Lambda_3)\cos\eta \\ F_{y-ump} = \frac{R_r L_r \pi}{4\mu_0} {F_j}^2 (2\Lambda_0\Lambda_1 + \Lambda_1\Lambda_2 + \Lambda_2\Lambda_3)\sin\eta \end{cases} \tag{31}$$

$$\Lambda_n = \begin{cases} \frac{\mu_0}{\delta_0}\frac{1}{\sqrt{1-\varepsilon^2}} & (n=0) \\ \frac{2\mu_0}{\delta_0}\frac{1}{\sqrt{1-\varepsilon^2}}\left(\frac{1-\sqrt{1-\varepsilon^2}}{\varepsilon}\right)^n & (n>0) \end{cases} \tag{32}$$

where $F_{x\text{-}ump}$ and $F_{y\text{-}ump}$ are the unbalanced magnetic pulls in x-direction and y-direction, respectively; R_r is the generator rotor radius; L_r is the generator rotor length; μ_0 is the air permeability; F_j is the fundamental magnetomotive force of the excitation current; ε is the relative eccentricity; δ_0 is the average air gap between stator and rotor; and η is the rotating angle.

(4) Hydraulic excitation force

When the hydro-turbine performs energy conversion, it also brings complicated hydraulic vibration problems to the HGSS. The reasons for this include many aspects, such as operation under non-design conditions, draft tube pressure pulsation, unequal sealing gaps, and excessive axial water thrust, etc. Zhuang [14] proposed an excitation force model on a single blade of the hydro-turbine runner. Superposition of the forces on all the blades of the hydro-turbine runner is the hydraulic excitation force, and its expression is

$$\begin{cases} F_{x-hef} = \frac{n_b\gamma C_y Q^2 F_b \cos(\beta_m - \lambda)}{8g\cos\lambda}\left[\frac{1}{(s_1\pi D_1 b_0 \sin\beta_1)^2} + \frac{1}{(s_2\pi D_2^2 \sin\beta_2)^2} + \frac{2\cos(\beta_2-\beta_1)}{s_1 s_2 \pi^2 D_1 D_2^2 b_0 \sin\beta_1 \sin\beta_2}\right]\cos\eta \\ F_{y-hef} = \frac{n_b\gamma C_y Q^2 F_b \cos(\beta_m - \lambda)}{8g\cos\lambda}\left[\frac{1}{(s_1\pi D_1 b_0 \sin\beta_1)^2} + \frac{1}{(s_2\pi D_2^2 \sin\beta_2)^2} + \frac{2\cos(\beta_2-\beta_1)}{s_1 s_2 \pi^2 D_1 D_2^2 b_0 \sin\beta_1 \sin\beta_2}\right]\sin\eta \end{cases} \tag{33}$$

$$\beta_m = \arcsin\left(\frac{2\left(s_1 D_1 b_0 + s_2 D_2^2\right)}{\sqrt{\left(\frac{s_2 D_2^2}{\sin\beta_1}\right)^2 + \left(\frac{s_1 D_1 b_0}{D_2^2 \sin\beta_2}\right)^2 + \frac{2 s_1 s_2 D_1 D_2^2 b_0 \cos(\beta_2 - \beta_1)}{\sin\beta_1 \sin\beta_2}}}\right) \tag{34}$$

$$\beta_1 = \arctan\left(\frac{2Q\tan\alpha_1}{\pi D_1^2 \omega s_1 b_0 \tan\alpha_1 - 2Q}\right) \tag{35}$$

where $F_{x\text{-}hef}$ and $F_{y\text{-}hef}$ are the hydraulic excitation forces in x-direction and y-direction, respectively; n_b is the number of runner blades; γ is the unit weight; $\lambda = \arctan(C_x/C_y)$; C_y is the lift coefficient; C_x is the drag coefficient; F_b is the maximum area of the blade; β_m is the direction angle of the relative average speed; s_1 and s_2 are the entrance excretion coefficient and exit excretion coefficient, respectively; D_1 and D_2 are the entrance diameter and exit diameter of hydro-turbine runner, respectively; b_0 is the height of guide vane; β_1 and β_2 are the blade entrance flow angle and the blade exit flow angle, respectively; and α_1 is the guide vane opening angle.

2.8. Model Validation

This study selects the real HGS parameters of Qinghai Province, China, to establish the model, as well as the comprehensive verification based on the operation characteristics and vibration characteristics of HGS. The HGS parameters of Qinghai Province in China are shown in Table 1.

Table 1. The HGS parameters of Qinghai province in China.

Model Parameter	Symbol	Value	Unit
Length of the tunnel	*TL*	5693	m
Length of the surge tank	*STL*	2.3	m
Length of the penstock behind the surge tank	*PBSTL*	84	m
Length of the sloping penstock	*SPL*	58.97	m
Length of the penstock behind the sloping penstock	*PBSPL*	562.44	m
Length of pipe 1/2/3	$PL_1/PL_2/PL_3$	360.6	m
Diameter of the tunnel	*TD*	3.2	m
Diameter of the surge tank	*STD*	6	m
Diameter of the surge tank impedance	*STID*	2.3	m
Diameter of the penstock behind the surge tank	*PBSTD*	3.2	m
Diameter of the sloping penstock	*SPD*	3	m
Diameter of the penstock behind the sloping penstock	*PBSPD*	3	m
Diameter of pipe 1/2/3	$PD_1/PD_2/PD_3$	1.73	m
Upstream water level	H_{start}	3456	m
Downstream water level	H_{end}	3252.05	m
Rated output	P_r	11	MW
Rated flow rate	n_r	600	rpm
Rated water head	Q_r	6.8	m^3/s
Runner diameter	D_1	1.4	m
Generator rotor diameter	D_2	3.144	m
Guide bearing stiffness	K	1×10^8	N/m
Generator rotor mass eccentricity	e_1	1×10^{-4}	m
Runner mass eccentricity	e_2	1×10^{-4}	m
Uniform air gap thickness	δ_0	2×10^{-2}	m
Air permeability	μ_0	$4\pi \times 10^{-7}$	H/m

First, the operation characteristics of HGSS #1, #2 and #3 in the simultaneous load rejection condition are simulated, and the simulation results are compared with the experimental results from [39]. Table 2 shows the comparison of the simulation results and the experiment results.

Table 2. The comparison of the simulation results and the experiment results.

Result	Upper and Lower Water Level (m)	HGSS	The Maximum Pressure Head at the Volute (m)	The Minimum Pressure Head at the Volute (m)	The Maximum Speed Rise Rate (%)	The Maximum and Minimum Surge Level in Surge Tank (m)
The simulation	3456.00 3252.05	#1 #2 #3	252.75 252.76 252.74	180.01 180.03 180.01	58.98 58.96 58.95	3471.7 3453.0
The experiment	3456.00 3252.05	#1 #2 #3	243.45 243.12 243.36	185.18 184.92 184.94	59.07 58.97 59.03	3476.29 3442.43

From Table 2, it can be seen that the maximum error of the maximum and minimum pressure at the volute are 3.9% and 2.79%, respectively; the maximum error of the maximum speed rise rate is 0.15%; and the error of the maximum and minimum surge in surge tank are 0.13% and 0.31%, respectively. The above comparisons show that the maximum error between the simulation and the experiment do not exceed 4%, and indicate that the established model is correct and reasonable in operation characteristics.

Second, 50%-, 75%-, and 100%-rated load conditions in an operable load area are selected to simulate the vibration characteristics of the HGS, and the simulation results are compared with the National Standard of China "*Specification installation of hydraulic turbine generator units. GB/T 5864-2003*" [40]. For the HGSS in this study, the allowable absolute vibration amplitudes of the upper guide bearing, the lower guide bearing, the flange, and the water guide bearing are 0.022 mm, 0.076 mm, 0.106 mm, and 0.2 mm, respectively. The vibration characteristics of different guide bearings and the flange are shown in Figure 8.

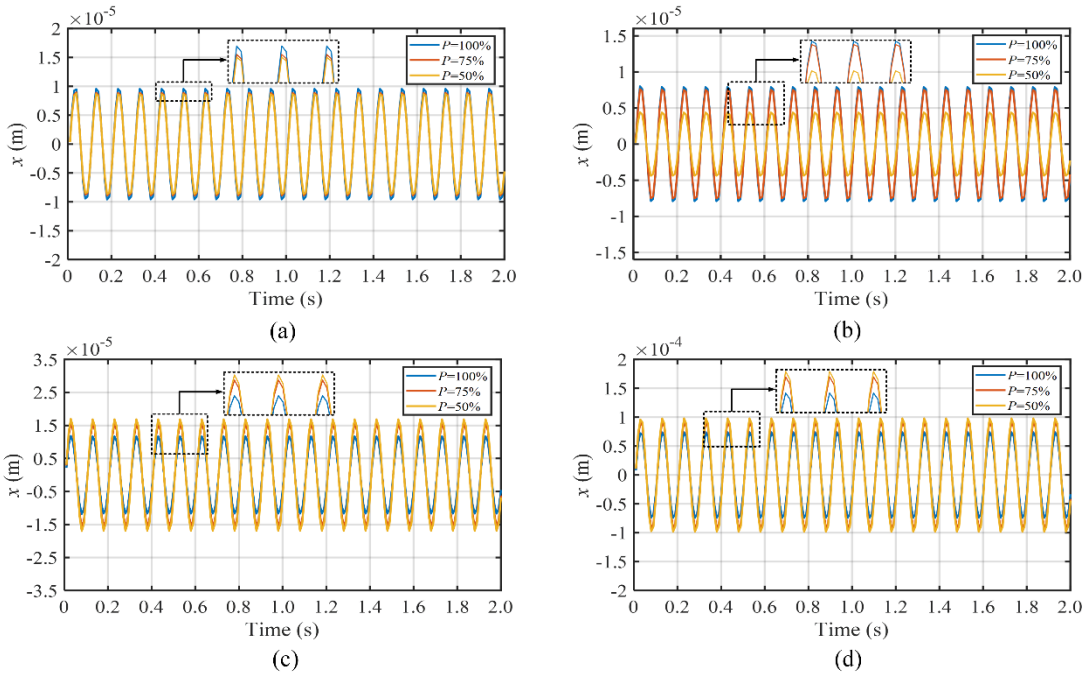

Figure 8. Vibration characteristics of different guide bearings and the flange. (**a**) The upper guide bearing; (**b**) the lower guide bearing; (**c**) the flange; (**d**) the water guide bearing.

The vibration characteristics of HGSS #1, #2, and #3 are similar, and HGSS #1 is used as an example. As shown in Figure 6, the upper guide bearing and the lower guide bearing are mainly affected by the mechanical unbalance force and UMP at the generator rotor, and the vibration amplitudes are the largest under the 100%-rated load condition, which are 0.0096 mm and 0.008 mm, respectively. The flange and the water guide bearing are mainly

affected by the hydraulic excitation force, and the vibration amplitudes are the largest under the 50%-rated load condition, which are 0.017 mm and 0.098 mm, respectively. The above results show that the vibration amplitudes of HGS do not exceed the allowable vibration amplitude in National Standard of China, and indicate that the established model is correct and reasonable in vibration characteristics.

3. Numerical Simulation and Result Analysis

3.1. Hydraulic Factors

(1) Sudden load increasing amount

For HGS in this study, 50–100%-rated load area is the operable area. Thus, in this subsection, the vibration characteristics of HGSS #1, #2, and #3 which collectively suddenly increase 30%, 40%, and 50%-rated load from the 50%-rated load (ΔP = 30%, ΔP = 40%, and ΔP = 50%) are analyzed. The operation and vibration characteristics of the hydro-turbine runner under different sudden load increasing amounts are shown in Figures 9–11, respectively.

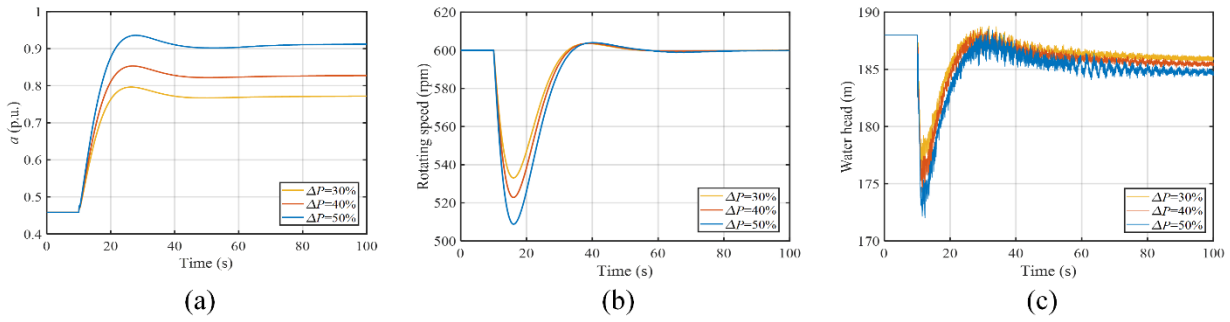

Figure 9. The operation characteristics of the hydro-turbine runner under different sudden load increasing amounts. (**a**) Guide vane opening; (**b**) rotating speed; (**c**) water head.

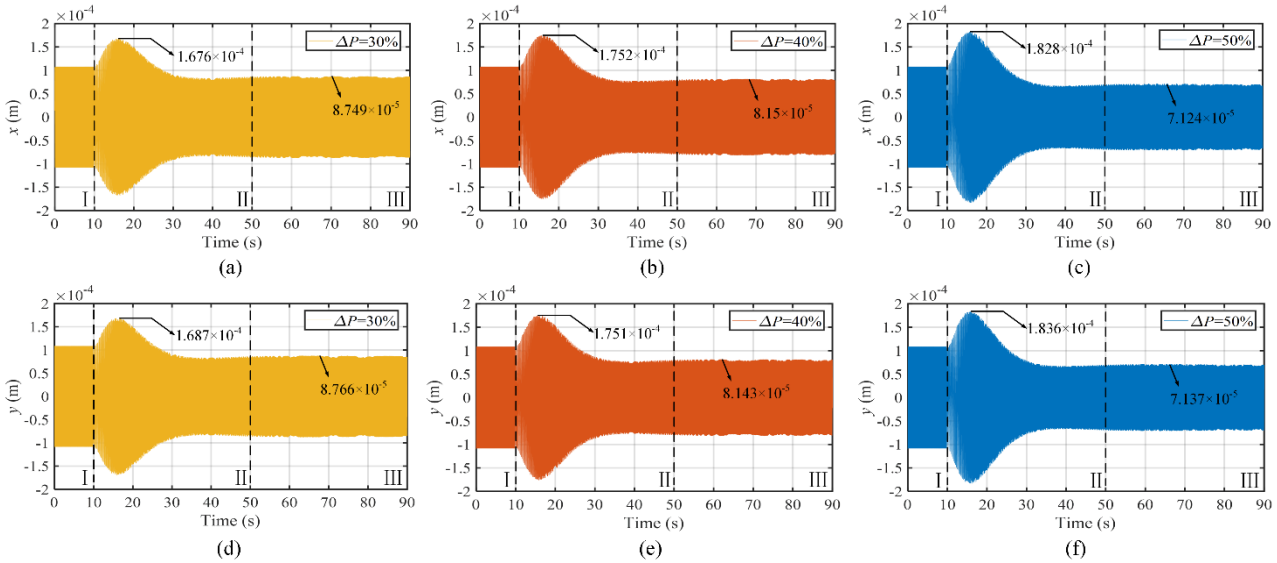

Figure 10. The time-domain figure of the hydro-turbine runner under different sudden load increasing amounts. (**a**–**c**) In *x*-direction; (**d**–**f**) in *y*-direction.

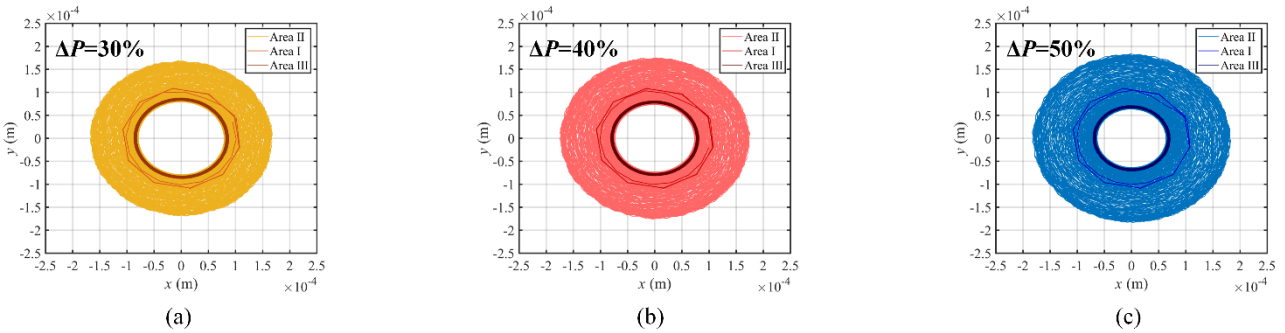

Figure 11. The axis trajectory of the hydro-turbine runner under different sudden load increasing amounts. (**a**) ΔP = 30%; (**b**) ΔP = 40%; (**c**) ΔP = 50%.

From Figure 9, the PID governor tracks the load change automatically, and opens the guide vane quickly. The rotating speed decreases by 11.16%, 12.87%, and 15.21%, and the water head decreases by 6.67%, 7.52%, and 8.46%, with the increase of sudden load increasing amount, respectively.

From Figure 10, it can be seen that Area I and Area III are the stable operating areas; Area II is the operating area of SLIP. When t = 16 s, the maximum vibration response occurs at the hydro-turbine runner. When ΔP = 50%, the vibration amplitudes of the hydro-turbine runner in x-direction and y-direction in Area II are the largest, which increase by 69.89% and 69.95%, compared with that of Area I, respectively. When ΔP = 30%, the vibration amplitudes of the hydro-turbine runner in x-direction and y-direction in Area III are the largest, which increase by 33.79% and 34.1%, compared with that of Area I, respectively. Thus, the hydraulic excitation force causes the vibration amplitude under a partial load to be greater than that under a rated load. In addition, as demonstrated in Figure 11, the greater the sudden load increasing amount, the greater the axis trajectory and vibration amplitude in Area II, and the smaller axis trajectory and vibration amplitude in Area III.

(2) Blade exit flow angle

When the Francis HGSS was operating in the non-optimal load condition area, the direction of the water flow from the blade exit had a circumferential component, which caused the vortex. Thus, in this subsection, the vibration characteristics of HGS under ΔP = 50% and the blade exit flow angles, taken as 0.05 rad, 0.1 rad, and 0.15 rad, are analyzed, respectively. The vibration characteristics of the hydro-turbine runner under different blade exit flow angles are shown in Figures 12 and 13.

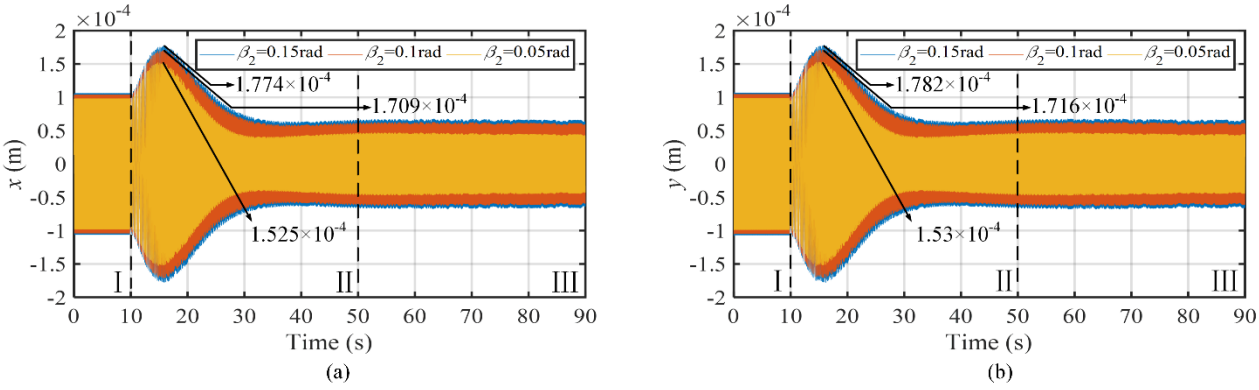

Figure 12. The time-domain figure of the hydro-turbine runner under different blade exit flow angles. (**a**) In x-direction; (**b**) in y-direction.

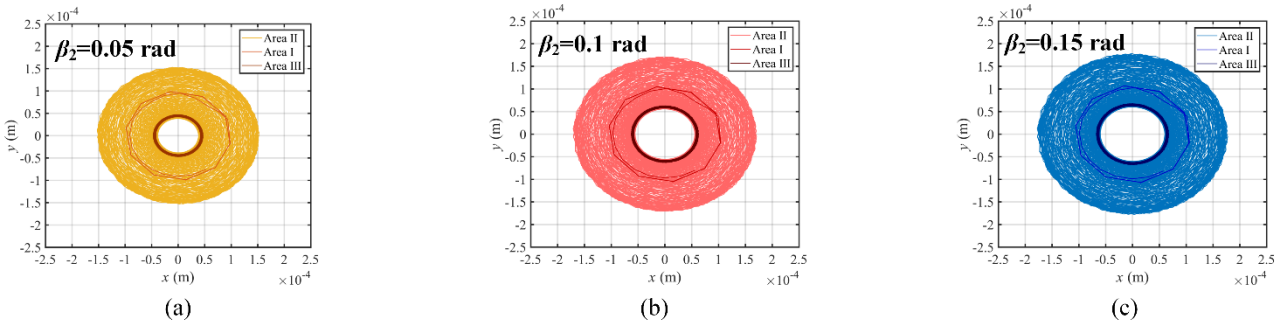

Figure 13. The axis trajectory of the hydro-turbine runner under different blade exit flow angles. (**a**) β_2 = 0.05 rad; (**b**) β_2 = 0.1 rad; (**c**) β_2 = 0.15 rad.

From Figures 12 and 13, when t = 15 s, the maximum vibration response occurs at the hydro-turbine runner. When β_2 = 0.15 rad, the vibration amplitudes of the hydro-turbine runner in x-direction and y-direction are the largest, which increase by 67.36% and 66.54%, compared with that of Area I, respectively. The greater the blade exit flow angle, the greater the axis trajectory and vibration amplitude of the hydro-turbine runner.

3.2. Mechanical Factors

(1) Mass eccentricity

Uneven mass distribution of the rotating parts caused by poor materials and insufficient installation accuracy is common, which causes the vibration of the HGS. Thus, in this subsection, the vibration characteristics of the HGS under ΔP = 50% and the mass eccentricities, taken as 0.4 mm, 0.6 mm, and 0.8 mm, are analyzed, respectively. The vibration characteristics of the generator rotor and the hydro-turbine runner under different mass eccentricities are shown in Figures 14 and 15.

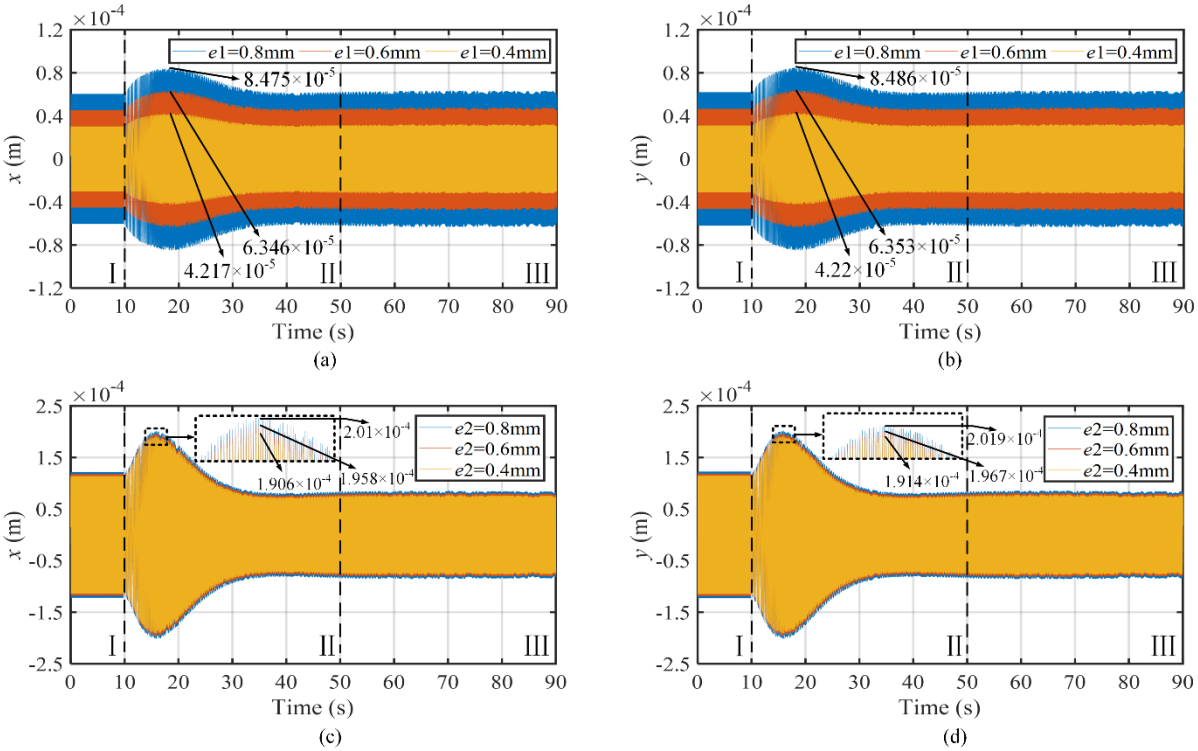

Figure 14. The time-domain figure of and under different mass eccentricities. (**a**,**b**) Generator rotor; (**c**,**d**) hydro-turbine runner.

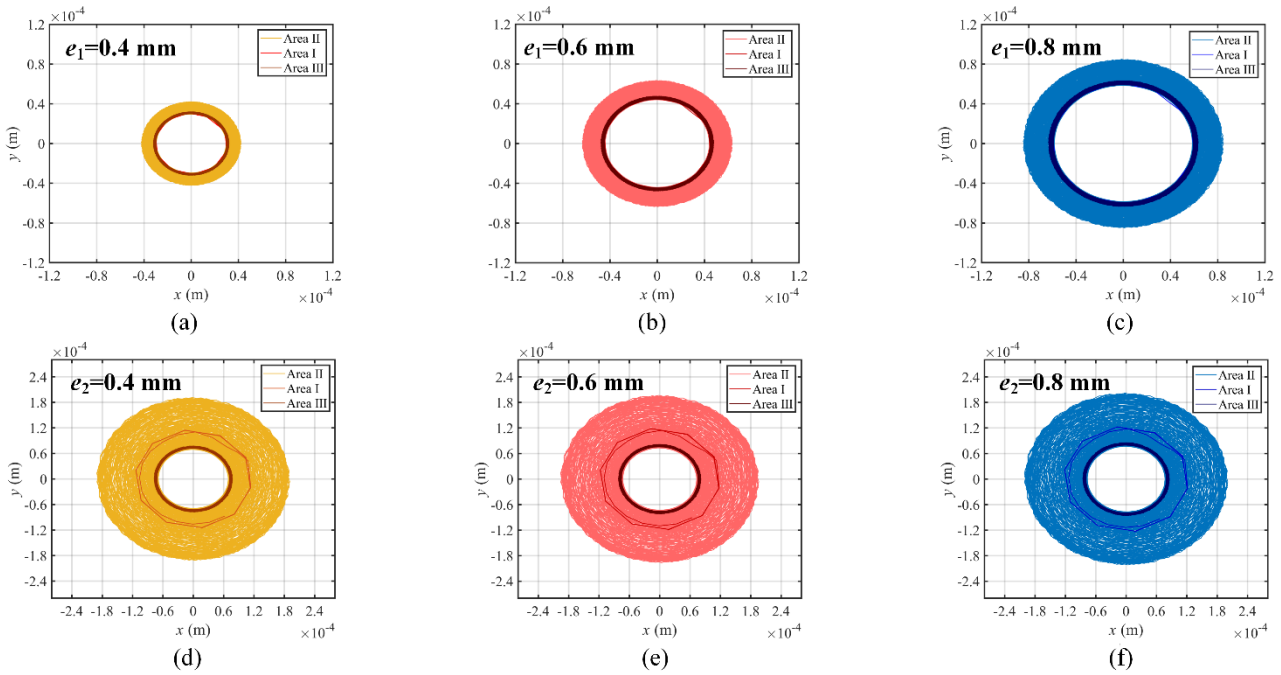

Figure 15. The axis trajectory of the generator rotor and the hydro-turbine runner under different mass eccentricities. (**a**–**c**) Generator rotor; (**d**–**f**) hydro-turbine runner.

From Figures 14 and 15, when t = 18 s and t = 15 s, the maximum vibration response occurs at the generator rotor and the hydro-turbine runner, respectively. When e = 0.8 mm, the vibration amplitudes of the generator rotor and the hydro-turbine runner in x-direction and y-direction are the largest, which increase by 40.71%, 37.25%, 65.3%, and 64.95%, compared with that of Area I, respectively. The axis trajectory and vibration amplitude of the HGS increase with mass eccentricity increase. In addition, the mass eccentricity has a great impact on the generator rotor, but a lesser impact on the hydro-turbine runner, as the hydro-turbine runner is greatly affected by hydraulic factors.

(2) Guide bearing stiffness

The guide bearing is used to bear the radial force during the operation, and limit the vibration of HGSS. Thus, the unreasonable guide bearing stiffness leads to the severe vibration of HGS. In this subsection, the vibration characteristics of the HGS under ΔP = 50% and different stiffnesses of the upper guide bearing, lower guide bearing, and water guide bearing are analyzed, respectively. The guide bearing stiffness is taken as 1.0×10^8 N $\times$ m^{-1}, 3.0×10^8 N $\times$ m^{-1}, and 5.0×10^8 N $\times$ m^{-1}, respectively. The vibration characteristics of the guide bearing under different stiffnesses are shown in Figures 16 and 17.

As demonstrated in Figures 16 and 17, the maximum vibration response of upper guide bearing, lower guide bearing, and water guide bearing occurs at t = 22 s, 17 s, and 15 s, respectively. When $K = 1.0 \times 10^8$ N $\times$ m^{-1}, the vibration amplitudes of the upper guide bearing, lower guide bearing, and water guide bearing in x-direction and y-direction are the largest, which increase by 41.24%, 36.35%, 63.54%, 60.01%, 70.46%, and 70.17%, compared with that of Area I, respectively. In conclusion, the stiffness of the water guide bearing has the greatest influence on vibration response, and the stiffness of the lower guide bearing has less influence on the vibration response than that of the upper guide bearing. The axis trajectory and vibration amplitude at guide bearing increase as guide bearing stiffness decreases.

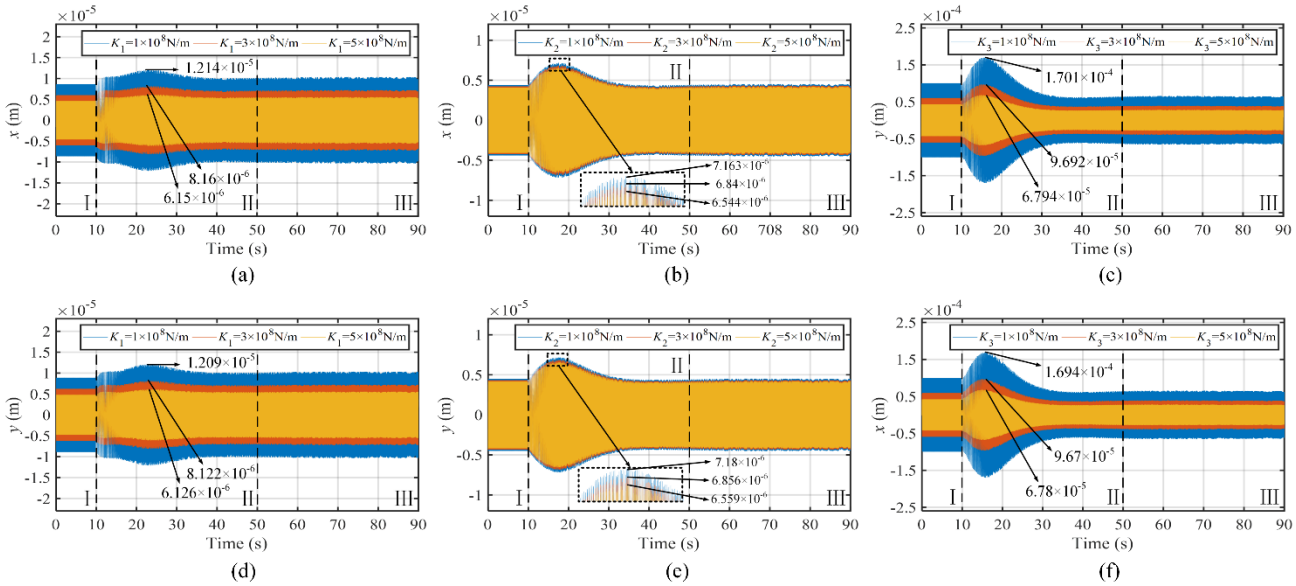

Figure 16. The time-domain figure under different stiffnesses. (**a**,**d**) Upper guide bearing; (**b**,**e**) lower guide bearing; (**c**,**f**) water guide bearing.

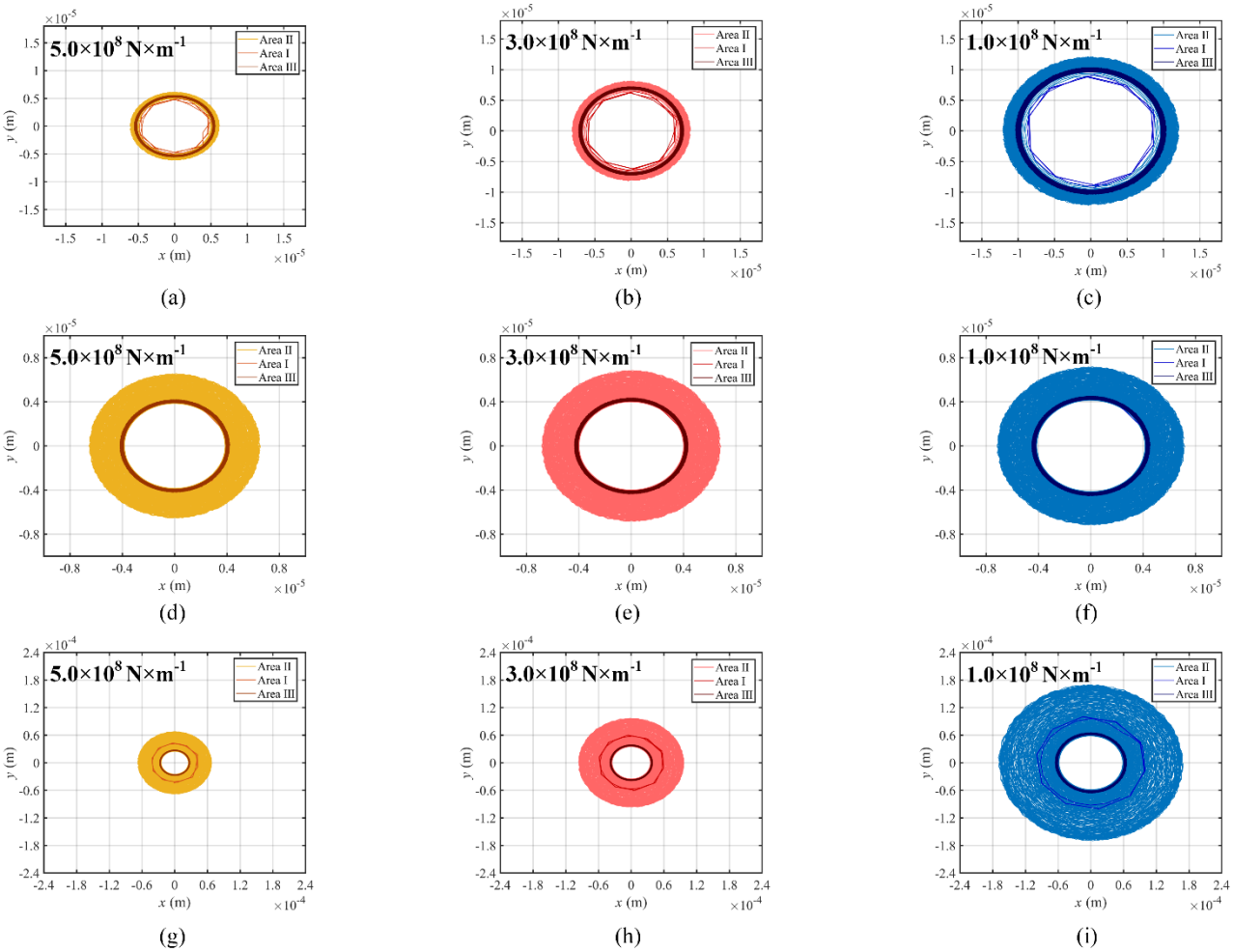

Figure 17. The axis trajectory under different stiffnesses. (**a**–**c**) Upper guide bearing; (**d**–**f**) lower guide bearing; (**g**–**i**) water guide bearing.

3.3. Electric Factors

(1) Excitation current

The change of excitation current causes the change of UMP, which leads to the vibration of the HGS. Thus, in this subsection, the vibration characteristics of HGS under ΔP = 50% and the excitation currents, taken as 50% I_j, 75% I_j, and 100% I_j, are analyzed, respectively. The vibration characteristics of the generator rotor under different excitation currents are shown in Figures 18 and 19.

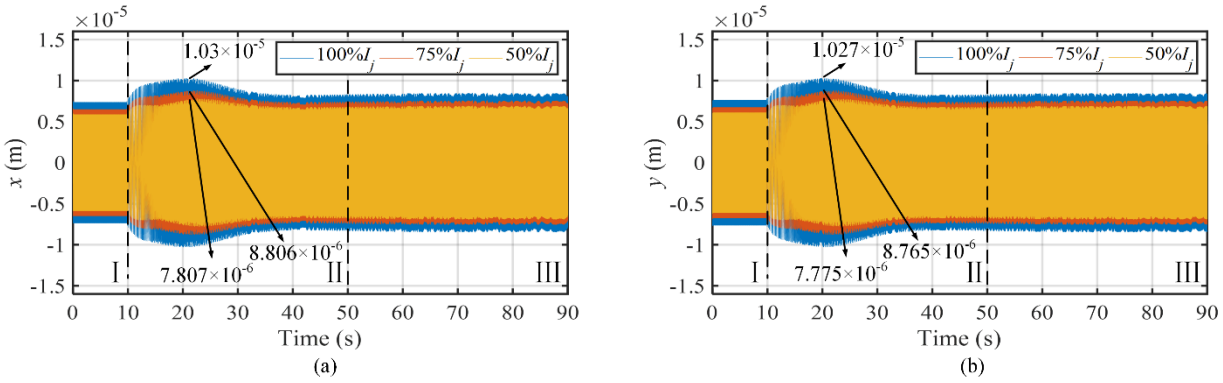

Figure 18. The time-domain figure of the generator rotor under different excitation currents. (**a**) In *x*-direction; (**b**) in *y*-direction.

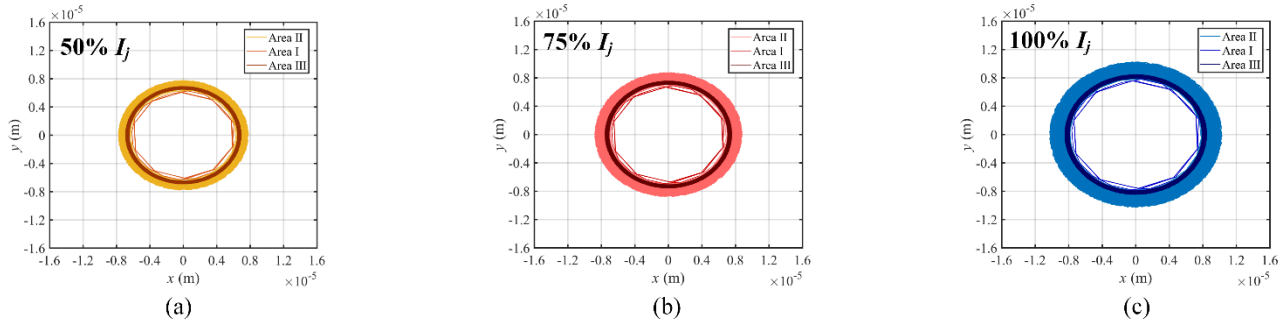

Figure 19. The axis trajectory of the generator rotor under different excitation currents. (**a**) 50% I_j; (**b**) 75% I_j; (**c**) 100% I_j.

As can be observed in Figures 18 and 19, when t = 21 s, the maximum vibration response occurs at the generator rotor. When 75% excitation current is conducted, the vibration amplitudes of the generator rotor in *x*-direction and *y*-direction are the largest, which increase by 40% and 34.67%, compared with that of Area I, respectively. The axis trajectory and vibration amplitude at the generator rotor increase as the excitation current increases.

(2) Average air gap between stator and rotor

An uneven air gap between the stator and rotor produces greater UMP, and aggravates the vibration of the HGSS. Thus, in this subsection, the vibration characteristics of HGS under ΔP = 50% and the average air gaps between the stator and rotor, taken as δ_0 = 20 mm, δ_0 = 30 mm, and δ_0 = 40 mm, are analyzed, respectively. The vibration characteristics of the generator rotor under different average air gaps between the stator and rotor are shown in Figures 20 and 21.

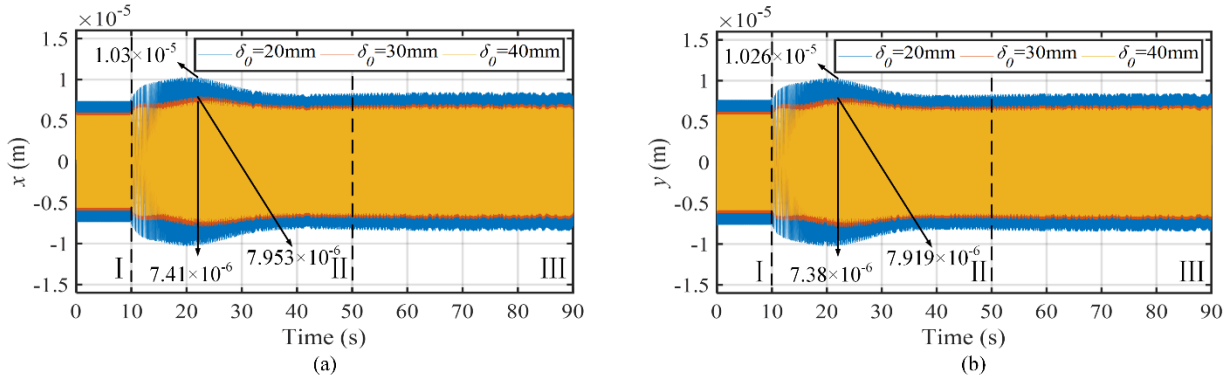

Figure 20. The time-domain figure of the generator rotor under different average air gaps between the stator and rotor. (**a**) In *x*-direction; (**b**) in *y*-direction.

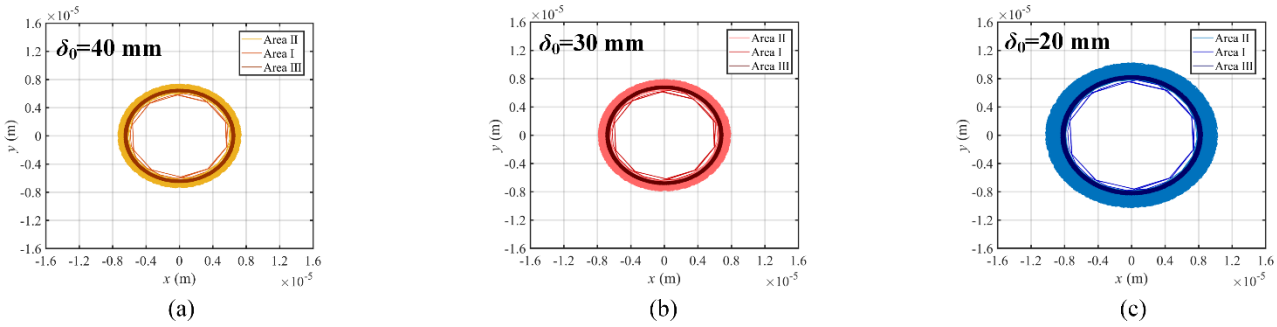

Figure 21. The axis trajectory of the generator rotor under different average air gaps between the stator and rotor. (**a**) δ_0 = 40 mm; (**b**) δ_0 = 30 mm; (**c**) δ_0 = 20 mm.

As demonstrated in Figures 20 and 21, when t = 21 s, the maximum vibration response occurs at the generator rotor. When δ_0 = 20 mm, the vibration amplitudes of the generator rotor in x-direction and y-direction are the largest, which increase by 40% and 34.54%, compared with that of Area I, respectively. The axis trajectory and vibration amplitude at the generator rotor increase as the average air gap between the stator and rotor decreases.

4. Conclusions

This study proposes a new transient nonlinear coupling model of HGS to analyze the influences of different HMEPs on the vibration characteristics of HGS in SLIP under SMSLPS. The main conclusions obtained are as follows:

(1) For hydraulic factors, the greater the sudden load increasing amount and blade exit flow angle, the greater the vibration of the hydro-turbine runner. The maximum vibration amplitude is increased by 69.95%, compared with that under stable operating conditions. Moreover, the vibration under a partial load is greater than that under a rated load. Hydraulic factors determine the tendency of vibration at hydro-turbine runner.

(2) For mechanical factors, the vibration of HGSS increases as mass eccentricity increases and guide bearing stiffness decreases. The maximum vibration amplitude is increased by 70.46%, compared with that under stable operating conditions. The mass eccentricity has a great impact on the generator rotor, but a lesser impact on the hydro-turbine runner. The influence of the water guide bearing stiffness on the vibration response is greater than that of the upper guide bearing and the lower guide bearing.

(3) For electric factors, the vibration of the generator rotor increases as the excitation current increases and the average air gap between the stator and rotor decreases. The maximum vibration amplitude is increased by 40%, compared with that under stable operating conditions.

More importantly, this study provides reasonable reference for the analysis of the nonlinear dynamic behavior of HGS in SLIP, and the stable operation of the hydropower station.

Author Contributions: Y.G.: conceptualization, methodology, software, writing—original draft, writing—reviewing and editing. X.L.: software, investigation, data curation, writing—review and editing. Z.N.: software, formal analysis, and data curation. Z.C.: visualization, writing—review and editing. L.L.: conceptualization, methodology and data curation. H.X.: software, writing—review and editing. D.C.: funding acquisition, supervision, writing—review and editing. All authors have read and agreed to the published version of the manuscript.

Funding: This work was supported by the scientific research foundation of the Natural Science Foundation of Shaanxi Province of China (2019JLP-24) and the Technology Innovation Team (2020TD-025).

Institutional Review Board Statement: Not applicable.

Informed Consent Statement: Not applicable.

Conflicts of Interest: The authors declare no conflict of interest.

Abbreviations

SLIP	Sudden Load Increasing Process
HMEPs	Hydraulic-Mechanical-Electric Parameter
HGSS	Hydro-turbine Generator Shafting System
UMP	Unbalanced Magnetic Pull
MOC	Method Of Characteristics
WNIM	Wilson-θ Numerical Integration Method
HGS	Hydroelectric Generating System
HTGS	Hydro-Turbine Governing System
SMSLPS	Single-Machine Single-Load Power System
WDS	Water Diversion System
RTMM	Riccati Transfer Matrix Method

References

1. Dehghani, M.; Riahi-Madvar, H.; Hooshyaripor, F.; Mosavi, A.; Shamshirband, S.; Zavadskas, E.K.; Chau, K.-W. Prediction of Hydropower Generation Using Grey Wolf Optimization Adaptive Neuro-Fuzzy Inference System. *Energies* **2019**, *12*, 289. [CrossRef]
2. Guo, W.C. A review of the hydraulic transient and dynamic behavior of hydropower plants with sloping ceiling tailrace tunnels. *Energies* **2019**, *12*, 3220. [CrossRef]
3. Sipahutar, R.; Bernas, S.M.; Imanuddin, M.S. Renewable energy and hydropower utilization tendency worldwide. *Renew. Sustain. Energy Rev.* **2013**, *17*, 13–15.
4. Singh, V.K.; Singal, S.K. Operation of hydro power plants-a review. *Renew. Sustain. Energy Rev.* **2017**, *69*, 610–619. [CrossRef]
5. Chazarra, M.; Garcia-Gonzalez, J.; Perez-Diaz, J.I.; Arteseros, M. Stochastic optimization model for the weekly scheduling of a hy-dropower system in day-ahead and secondary regulation reserve markets. *Electr. Power Syst. Res.* **2016**, *130*, 67–77. [CrossRef]
6. Trivedi, C. Study of pressure pulsations in a Francis turbine designed for frequent start-stop. *J. Energy Resour. Technol.* **2021**, *143*, 1–24. [CrossRef]
7. Guo, P.C.; Zhang, H.; Gou, D.M. Dynamic characteristics of a hydro-turbine governing system considering draft tube pressure pulsation. *IET Renew. Power Gener.* **2020**, *14*, 1210–1218. [CrossRef]
8. Li, H.; Chen, D.; Tolo, S.; Xu, B.; Patelli, E. Hamiltonian Formulation and Analysis for Transient Dynamics of Multi-Unit Hydropower System. *J. Comput. Nonlinear Dyn.* **2018**, *13*, 101004. [CrossRef]
9. Pan, Z.; Dai, Y. The influence of the overspeed protection control for the isolated grid stability. In Proceedings of the International Conference on Power System Technology, Hangzhou, China, 24–28 October 2010; pp. 1–6.
10. Yan, D.L.; Wang, W.Y.; Chen, Q.J. Nonlinear modeling and dynamic analyses of the hydro-turbine governing system in the load shedding transient regime. *Energies* **2018**, *11*, 1244. [CrossRef]
11. Liao, C.W.; Zhang, J.S. Analysis of the breast wall collapse of the surge shaft of Tianshengqiao-II hydropower station. *Water Power* **1994**, *10*, 24–26. (In Chinese)
12. Ishida, Y.; Liu, J.; Inoue, T.; Suzuki, A. Vibrations of an Asymmetrical Shaft with Gravity and Nonlinear Spring Characteristics (Isolated Resonances and Internal Resonances). *J. Vib. Acoust. Trans. ASME* **2008**, *130*, 041004. [CrossRef]
13. Xu, B.; Chen, D.; Behrens, P.; Ye, W.; Guo, P.; Luo, X. Modeling oscillation modal interaction in a hydroelectric generating system. *Energy Convers. Manag.* **2018**, *174*, 208–217. [CrossRef]

14. Zhuang, K.; Gao, C.; Li, Z.; Yan, D.; Fu, X. Dynamic Analyses of the Hydro-Turbine Generator Shafting System Considering the Hydraulic Instability. *Energies* **2018**, *11*, 2862. [CrossRef]
15. Favrel, A.; Junior, J.G.P.; Müller, A.; Landry, C.; Yamamoto, K.; Avellan, F. Swirl number based transposition of flow-induced mechanical stresses from reduced scale to full-size Francis turbine runners. *J. Fluids Struct.* **2020**, *94*, 102956. [CrossRef]
16. Al-Hussain, K.M.; Redmond, I. Dynamic response of two rotors connected by rigid mechanical coupling with parallel misalignment. *J. Sound Vib.* **2002**, *249*, 483–498. [CrossRef]
17. Yong-Wei, T.; Jian-Gang, Y. Research on vibration induced by the coupled heat and force due to rotor-to-stator rub. *J. Vib. Control* **2011**, *17*, 549–566. [CrossRef]
18. Calleecharan, Y.; Aidanpaa, J.O. Dynamics of a hydropower generator subjected to unbalanced magnetic pull. *Proc. Inst. Mech. Eng. Part C J. Mech. Eng. Sci.* **2011**, *225*, 2076–2088. [CrossRef]
19. Xu, Y.; Li, Z.H. Computational model for investigating the influence of unbalanced magnetic pull on the radial vibration of large hydro-turbine generators. *J. Vib. Acoust. Trans. ASME* **2012**, *134*, 051013. [CrossRef]
20. Li, H.; Chen, D.; Zhang, X.; Wu, Y. Dynamic analysis and modelling of a Francis hydro-energy generation system in the load rejection transient. *IET Renew. Power Gener.* **2016**, *10*, 1140–1148. [CrossRef]
21. Zeng, Y.; Zhang, L.; Guo, Y.; Qian, J.; Zhang, C. The generalized Hamiltonian model for the shafting transient analysis of the hydro turbine generating sets. *Nonlinear Dyn.* **2014**, *76*, 1921–1933. [CrossRef]
22. Zhang, L.; Wu, Q.; Ma, Z.; Wang, X. Transient vibration analysis of unit-plant structure for hydropower station in sudden load increasing process. *Mech. Syst. Signal Process.* **2019**, *120*, 486–504. [CrossRef]
23. Wu, Q.Q.; Zhang, L.K.; Ma, Z.Y. A model establishment and numerical simulation of dynamic coupled hydraulic–mechanical–electric–structural system for hydropower station. *Nonlinear Dyn.* **2016**, *87*, 459–474. [CrossRef]
24. Guo, B.Q.; Xu, B.B.; Chen, D.Y.; Li, F.; Behrens, P.; Egusquiza, E. Vibration characteristics of the hydroelectric generating systems during load rejection transient process. *J. Comput. Nonlinear Dyn.* **2019**, *14*, 071006. [CrossRef]
25. Rezghi, A.; Riasi, A. Sensitivity analysis of transient flow of two parallel pump-turbines operating at runaway. *Renew. Energy* **2016**, *86*, 611–622. [CrossRef]
26. Chaudhry, M.H. Characteristics and finite-difference methods. *Appl. Hydraul. Transients* **2014**, *94*, 65–113.
27. Riasi, A.; Tazraei, P. Numerical analysis of the hydraulic transient response in the presence of surge tanks and relief valves. *Renew. Energy* **2017**, *107*, 138–146. [CrossRef]
28. Karlsson, M.; Aidanpää, J.-O.; Perers, R.; Leijon, M. Rotor Dynamic Analysis of an Eccentric Hydropower Generator with Damper Winding for Reactive Load. *J. Appl. Mech.* **2007**, *74*, 1178–1186. [CrossRef]
29. Rezghi, A.; Riaasi, A.; Tazraei, P. Multi-objective optimization of hydraulic transient condition in a pump-turbine hydropower considering the wicket-gates closing law and the surge tank position. *Renew. Energy* **2020**, *148*, 478–491. [CrossRef]
30. Yang, W.; Yang, J.; Guo, W.; Zeng, W.; Wang, C.; Saarinen, L.; Norrlund, P. A Mathematical Model and Its Application for Hydro Power Units under Different Operating Conditions. *Energies* **2015**, *8*, 10260–10275. [CrossRef]
31. Guo, W.C.; Yang, J.D. Stability performance for primary frequency regulation of hydro-turbine governing system with surge tank. *Appl. Math. Model.* **2017**, *54*, 446–466. [CrossRef]
32. Hou, J.; Li, C.; Tian, Z.; Xu, Y.; Lai, X.; Zhang, N.; Zheng, T.; Wu, W. Multi-Objective Optimization of Start-up Strategy for Pumped Storage Units. *Energies* **2018**, *11*, 1141. [CrossRef]
33. Li, C.; Zhang, N.; Lai, X.; Zhou, J.; Xu, Y. Design of a fractional-order PID controller for a pumped storage unit using a gravitational search algorithm based on the Cauchy and Gaussian mutation. *Inf. Sci.* **2017**, *396*, 162–181. [CrossRef]
34. Huang, S.; Chi, X.; Xu, Y.; Sun, Y. Dynamic characteristics of coupling shaft system in tufting machine based on the Riccati whole transfer matrix method. *Proc. Inst. Mech. Eng. Part C J. Mech. Eng. Sci.* **2016**, *231*, 356–371. [CrossRef]
35. Yin, S.H. Vibration of a simple beam subjected to a moving sprung mass with initial velocity and constant acceleration. *Int. J. Struct. Stab. Dyn.* **2016**, *16*, 176–185. [CrossRef]
36. Cui, Y.; Liu, Z.; Wang, Y.; Ye, J. Nonlinear Dynamic of a Geared Rotor System with Nonlinear Oil Film Force and Nonlinear Mesh Force. *J. Vib. Acoust.* **2012**, *134*, 041001. [CrossRef]
37. Gao, H.; Song, W. Analysis on unbalance vibration and compensation for maglev flywheel. *Int. J. Appl. Electromagn. Mech.* **2016**, *50*, 177–187. [CrossRef]
38. Zhang, L.; Ma, Z.; Wu, Q.; Wang, X. Vibration analysis of coupled bending-torsional rotor-bearing system for hydraulic generating set with rub-impact under electromagnetic excitation. *Arch. Appl. Mech.* **2016**, *86*, 1665–1679. [CrossRef]
39. Wang, M.H. Study on Calculation of Transition Process of Long-Loaded Hydropower Station. Master's Thesis, North China University of Water Resources and Electric Power, Zhengzhou, China, 2019.
40. General Administration of Quality Supervision. *Specification Installation of Hydraulic Turbine Generator Units*; GB/T 8564-2003; China Standards Press: Beijing, China, 2004. (In Chinese)